ACS POLYMERS Au
AN OPEN ACCESS JOURNAL OF THE AMERICAN CHEMICAL SOCIETY

pubs.acs.org/polymerau

Article

Fracture in Silica/Butadiene Rubber: A Molecular Dynamics View of Design–Property Relationships

Alessio David, Ugo Tartaglino, Mosè Casalegno, and Guido Raos*

Cite This: *ACS Polym. Au* 2021, 1, 175–186

Read Online

ACCESS | Metrics & More | Article Recommendations

ABSTRACT: Despite intense investigation, the mechanisms governing the mechanical reinforcement of polymers by dispersed nanoparticles have only been partially clarified. This is especially true for the ultimate properties of the nanocomposites, which depend on their resistance to fracture at large deformations. In this work, we adopt molecular dynamics simulations to investigate the mechanical properties of silica/polybutadiene rubber, using a quasi-atomistic model that allows a meaningful description of bond breaking and fracture over relatively large length scales. The behavior of large nanocomposite models is explored systematically by tuning the cross-linking, grafting densities, and nanoparticle concentration. The simulated stress–strain curves are interpreted by monitoring the breaking of chemical bonds and the formation of voids, up to complete rupture of the systems. We find that some chemical bonds, and particularly the S–S linkages at the rubber–nanoparticle interface, start breaking well before the appearance of macroscopic features of fracture and yield.

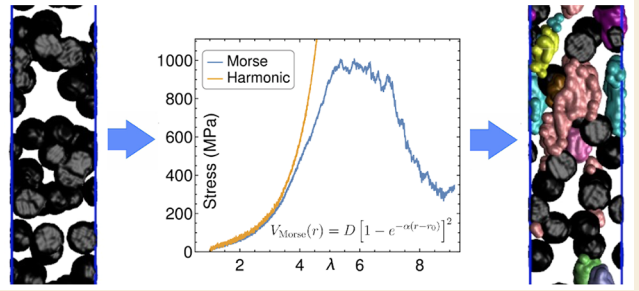

KEYWORDS: *Molecular dynamics, Fracture, Rubber reinforcement, Silica nanoparticles, Bond breaking*

INTRODUCTION

Polymer nanocomposites (PNCs) combine the well-known properties of polymers with the reinforcing, electrical, thermal, or optical features of different nanosized fillers.[1] Due to the high area/volume ratio of these fillers—provided the nanoparticles (NPs) are well dispersed and there is good mechanical coupling between them and the polymer—a significant fraction of the matrix belongs to an interfacial region with properties distinct from those in the bulk.[2] This produces exotic properties, which may emerge even at relatively low NP loadings. Virtually all polymers can be modified by incorporating suitable NPs, but this concept has been known and exploited for a long time in elastomers for automotive tires and other rubber goods, in fact long before the "nano" keyword became fashionable. In this case the fillers are either carbon black or silica, and the target is the enhancement of a complex combination of mechanical properties (elastic modulus, resistance to tear and abrasion, control of energy dissipation at low or high frequencies, etc.).[3,4]

The theory of rubber elasticity is now a mature subject,[5−9] thanks also to inputs from computer simulation that have helped clarify the role of topological constrains and defects.[10−12] The same cannot be said of the ultimate mechanical properties of polymer networks and especially of filled elastomers, which involve their resistance to fracture.[13] Although these materials are extensively employed in industry, the mechanisms of reinforcement are still not completely understood.[14] For sure, the usual assumption (for classical composites)[15] that the material consists of two distinct and well-defined phases is untenable, due to the extensive alteration of the polymer properties at the interface with the NPs.[16−21] The complex surface structure and chemistry of these fillers may be crucially important, especially with respect to the polymer dynamics.[22−25]

Molecular simulations of PNCs have increased significantly in recent years, as their complexity can now be approached thanks to advances in high-performance computing.[26−28] Molecular dynamics (MD)[29] and other particle-based mesoscale methods[30−32] are well suited to explore the behavior of these materials, revealing details that are not readily accessible to experiments. Today, most MD simulation of rubbery PNCs are still carried out with generic coarse-grained models, which aim at simplicity and a general understanding, rather than quantitative, predictive modeling.[33−39] Despite their greater complexity, in recent years there have been some notable atomistic (i.e., chemically detailed) simulations of silica-filled rubber networks,[40−42] which in principle may be used to address system-specific questions.

Received: August 6, 2021
Revised: September 23, 2021
Accepted: September 23, 2021
Published: October 8, 2021

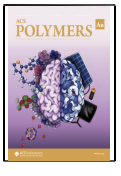

Table 1. Lennard−Jones Parameters for the Nonbonded Interactions[a]

	CH_2		CH		Q^3		Q^4		S	
	ε	σ	ε	σ	ε	σ	ε	σ	ε	σ
CH_2	0.0936	4.009								
CH	0.1015	3.792	0.1000	3.385						
Q^3	0.0967	4.780	0.1000	4.393	0.1000	5.700				
Q^4	0.1676	4.200	0.1732	3.859	0.1732	5.008	0.3000	4.400		
S	0.1529	3.772	0.1581	3.467	0.1581	4.498	0.2739	3.952	0.2500	3.550

[a]Units for ε and σ are kcal/mol and Å, respectively.

This paper is devoted to the simulation of the mechanical properties of polybutadiene networks incorporating silica nanoparticles. This combination of materials has practical interest,[43] but it has also been adopted in more fundamental studies of reinforcement.[44] We have combined elements from our previous papers on silica[45] and butadiene networks[46] into a coherent model, adding the possibility of bond scission in order to model large deformations and fracture. Our original motivation for adopting a united-atom model for the polymer, instead of a more coarse grained representation, was precisely the desire to model bond breaking and failure.[47] We point out that, although polymer fracture has been modeled using generic bead-and-spring models,[48−50] their applicability to extreme mechanical situations in not really known. For example, although there are "recipes" for mapping bead-and-spring models to commercial polymers,[51] we are not aware of any "recipe" for choosing the coarse-grained bond dissociation potential for those polymers (to replace the original finitely extensible but unbreakable bond potential). At the other extreme, one could have adopted one of the emerging "reactive" force fields, such as ReaxFF[52] or AIREBO.[53] However, the computational cost of these potentials (at least 10 times greater than that of a simulation based on conventional atomistic force fields)[54] would have hampered the treatment of large systems containing hundreds of NPs and hundreds of thousands of atoms.

The next section introduces our model, providing crucial implementation details. Next, we discuss the results of our simulations. When planning them, we adopted a material design exploration that is typical of the industrial mindset. By changing and studying the effect of one system parameter at a time, we have attempted an optimization of the material by maximizing certain target properties. The last part of the results section establishes a connection between the stress−strain curves and different modes of damage of the materials: namely, the breaking of chemical bonds and the formation and growth of voids within the matrix. Conclusions follow.

MODEL AND METHODS

Our model systems consist of silica nanoparticles within a poly(1,4-*cis*-butadiene) (PB) matrix. The polymer chains are 100 monomers long (i.e., 400 carbons), and they are cross-linked by simulating the reaction with sulfur dimers using the protocols described in our previous work.[46] The nanoparticles have a diameters of 4 nm, and they are chemically bonded to the polymer by short linker chains, mimicking the role of silane coupling agents. All simulations were carried out with the LAMMPS code, exploiting acceleration with graphical processing units (GPUs).[55] The results were visualized with VMD[56] and analyzed with in-house scripts. Below we provide some further details, focusing especially on aspects that were not covered in our previous papers.[45,46]

Force Fields

The force field parameters for PB were borrowed from a previous united-atom model.[57,58] Those for the sulfur atoms and the linker chains were derived from the united-atom version of OPLS.[59] The silica nanoparticles are described by a coarse-grained model, which suppresses the oxygen atoms leaving only Si-centered "superatoms" or beads.[45] This simple coarse-graining strategy reduces the number of atoms and effectively eliminates all electrostatic interactions, as all the atoms and particles have a zero charge. The absence of long-range electrostatic interactions produces significant acceleration in the simulations.

The silica beads are of two types: those within the bulk of the material are "non-polar", whereas those at the surface may be "polar" if they derive from Si atoms carrying an −OH group (silanols).[60] Following the NMR terminology, they will be denoted as Q^4 and Q^3, respectively. Bonding interactions among these beads need not be specified, since each NP is treated as a rigid body, capable only of translation and rotation. Their nonbonded interactions with other silica beads and with the polymer are described by truncated and shifted Lennard−Jones potentials—the function used also for the polybutadiene force field[45]

$$V_{ij}(r) = \begin{cases} 4\varepsilon_{ij}\left[\left(\frac{\sigma_{ij}}{r}\right)^{12} - \left(\frac{\sigma_{ij}}{r}\right)^{6}\right] + V_{ij}^{c} & \text{for } r < r_c \\ 0 & \text{for } r \geq r_c \end{cases} \quad (1)$$

where the V_{ij}^c values are constants ensuring continuity of the potential functions at the nonbonded cutoff r_c = 12 Å (identical for all interactions). The Lennard−Jones parameters for the silica beads were selected by matching the density fluctuations of the polymer sandwiched between reference atomistic and coarse-grained silica walls.

With the exception of the CH_2···CH interactions,[57,58] we used geometric mixing rules to derive both the ε_{ij} and the σ_{ij} parameters for unlike atoms, as was done also in the OPLS force field.[59] Note, however, that the parameters for silica−silica interactions were not optimized; rather, they were derived from those for silica−carbon interactions by an "inverse mixing" rule:

$$\varepsilon_{XX} = \frac{\varepsilon_{iX}^2}{\epsilon_{ii}}\sigma_{XX} = \frac{\sigma_{iX}^2}{\sigma_{ii}} \quad (2)$$

where X denotes a Q^3 or Q^4 particle and i any of the others. Because of this choice, the representation of direct nonbonded interactions among the Si beads may not be realistic. However, it is not critically important as long as one simulates well-dispersed morphologies with no direct NP−NP contacts. All the Lennard−Jones parameters of the model are given in Table 1.[45,61]

In order to model fracture phenomena, the possibility of covalent bond dissociation was explicitly included. To this end, the commonly adopted harmonic potential terms for bond stretching were replaced with Morse potential functions

$$V_{\text{Morse}}(r) = D[1 - e^{-\alpha(r-r_0)}]^2 \quad (3)$$

where D represents the bond dissociation energy and r_0 the equilibrium distance. All bond stretching parameters are given in Table 2, while those for bond bending and torsions can be found in the original publications.[57−59] Values for the bond dissociation energy were taken

https://doi.org/10.1021/acspolymersau.1c00023
ACS Polym. Au 2021, 1, 175−186

Table 2. List of Morse Potential Parameters

bond type	D (kcal/mol)	α (Å^{-1})	r_0 (Å)	r_{cb} (Å)
CH_2-CH_2, $CH-CH_2$	83.6	1.99	1.54	4.37
CH=CH	146.0	1.88	1.34	4.64
S−S	53.8	1.76	2.04	5.00
CH−S	62.1	1.89	1.81	4.64

from an extensive compilation of experimental data,[62] using a simple criterion of "chemical similarity". Note the order of the bond dissociation energies: S−S < C−S < C−C ≪ C=C. As we shall see, the bonds tend to dissociate in this order under deformation. Bond distances were taken to be equal to those from the corresponding harmonic bond potentials. Finally, the α parameter determines the curvature of the potential energy around the equilibrium distance. Its values were chosen to reproduce the force constants of the harmonic potentials entering the original force fields:

$$\alpha = \sqrt{\frac{k_{harm}}{2D}} \tag{4}$$

A cutoff distance r_{cb} for the bonds was set according to the condition

$$V_{Morse}(r_{cb}) = D - RT \tag{5}$$

where RT = 0.592 kcal/mol at 298 K. According to this criterion there is a different cutoff for every bond type. Bonds reaching an extension beyond the cutoff distance were permanently deleted from the bond list. Unlike a fully reactive force field, our model does not allow the possibility of bond formation. This should not matter much in our simulations, which aimed at observing a one deformation half-cycle, up to full rupture of the nanocomposites.

A special treatment was necessary for the bonds between the first carbon of the linker molecules and the coarse-grained silicon atoms. This type of bond must implicitly account for the oxygen atoms between the silicon and the carbon. The equilibrium length of these Si(O)C "bonds" was set equal to 2.75 Å. This value was obtained by quantum chemical calculations on a model compound. Specifically, we performed B3LYP/def2-SVP geometry optimizations of tetraethoxysilane, using version 4.2.1 of the ORCA code.[63] For simplicity, we chose to model the coarse-grained bonds with a harmonic potential instead of the Morse potential. This bond potential is simpler to handle, and it brings the additional benefit of smoothing the transition from the perfectly rigid filler to the highly deformable and breakable rubber phase. The force constant of the Si(O)C bonds was set equal to 50 kcal mol^{-1} Å^{-2}. This relatively low value reflects the fact that deformation of these coarse-grained bonds may occur by opening the Si−O−C bond angles, rather than by stretching the Si−O and O−C bond lengths.

Nanoparticle Generation

Industrial silica NPs are manufactured with a Stöber-like sol−gel process[64] or from pyrolysis that generates fumed silica.[18] Typically, the diameter of the primary silica particles is in the 10−15 nm range, somewhat smaller that the unperturbed end-to-end distance of lightly cross linked PB chains (about 26 nm for 1000 monomers, using the data of Fetters et al.[65]). Here we have simulated not only smaller nanoparticles (4 nm diameter) but also higher degrees of cross-linking, due to the relatively short length of the precursor chains.[46]

Our first attempts to generate the NPs from an amorphous silica model within the VMD code[56] resulted in structures characterized by anomalous cavities and many "dangling" silicon atoms, unlikely to be present in equilibrated NP structures. To circumvent this issue, the NPs were generated by cutting spheres with a diameter of 4 nm out of a crystalline sample of α-cristobalite. This choice is motivated by recent studies,[64] confirming the adequateness of such a material in relation to the surface properties of small nanoparticles. The silicon atoms were assigned types Q^4 and Q^3 on the basis of their connectivity, and then the oxygen atoms were deleted. The resulting Q^3 surface density was 2.78 nm^{-2}.

The NPs were chemically bonded to the polymer matrix by linkers mimicking the Si-69 silane bis(triethoxysilylpropyl) tetrasulfide.[66] Figure 1 illustrates the chemical structure of Si-69 and its mode of interaction with the filler and the elastomer. The scheme highlights the double role of silanes: namely, improving the dispersion of the silica nanoparticles by increasing their hydrophobicity and suppressing the hydrogen bonds between the silanol groups populating their surfaces, and enhancing the mechanical coupling with the polymer by covalent bonding. The formation of covalent bonds between the linker and the NP proceeds by hydrolysis and elimination of a part of the ethanol moieties. Covalent bonds between Si-69 units bound to the NP surface and the polymer form subsequently, following cleavage of one of the central S−S bonds during the curing of the elastomer. Within our model, a coarse-grained representation of Si-69 linkers was obtained by three consecutive united-atom CH_2 beads, directly attached to a Q^3 silicon at one end and bearing a disulfur unit at the other end. The terminal disulfur units mimic the structure of Si-69 immediately after scission of the central S−S bond, before the final bonding to the rubber matrix. In analogy with the degrees of functionalization adopted industrially, the linkers were bound to 20% of Q^3 beads,[67] yielding a density of 0.56 linkers/nm^2. Subsequently, the disulfur groups were chemically bonded to the polymer in the vulcanization stage, concurrently with the creation of the sulfur cross-links between the chains (see below). Each silica NP contains 928 beads, including the silane linkers. Figure 2 shows one of them.

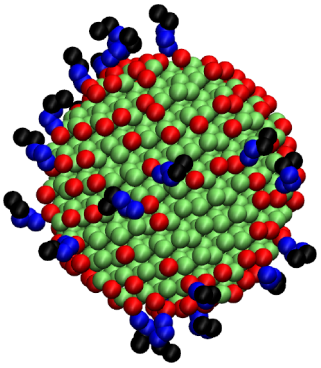

Figure 2. Sketch of a silica NP. Green, red, blue, and black beads refer to Q^4, Q^3, CH_2, and S units, respectively.

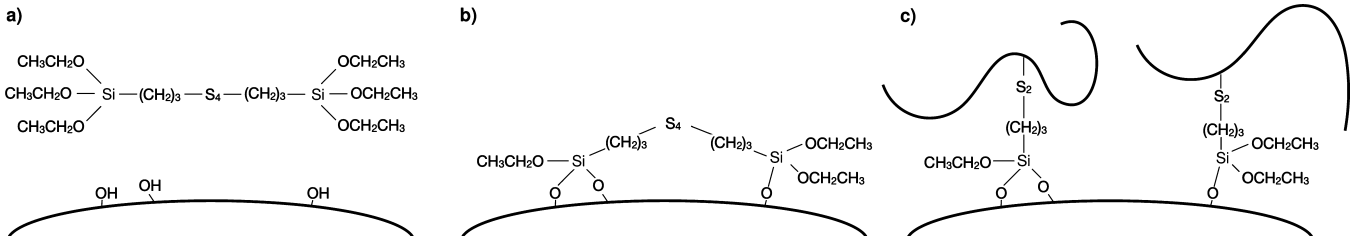

Figure 1. Picture showing the three stages of bonding of Si-69 to the NP surface and the polymer: (a) physical absorption; (b) grafting to the filler; (c) bonding to the polymer during curing.

https://doi.org/10.1021/acspolymersau.1c00023
ACS Polym. Au 2021, 1, 175−186

Table 3. Composition of the Simulated Systems

	[grafting coverage (nm^{-2}), NP concentration (vol %), CL density (SS/chain)]								
	[0, 0, 2]	[0, 20, 2]	[0.14, 20, 2]	[0.56, 20, 2]	[0.56, 6, 2]	[0.56, 14, 2]	[0.56, 20, 1.6]	[0.56, 20, 1.2]	[0.14, 6, 1.6]
silica NPs (count)	0	100	100	100	30	70	100	100	30
polymer chains (count)	1388	1388	1388	1388	1631	1492	1388	1388	1631
beads (count)	560752	653552	653552	653552	687164	667728	653552	653552	687164
av box length (nm)	23.6	26.2	26.2	26.1	25.7	25.1	24.6	24.6	25.7
av box volume (nm^3)	$1.31{\cdot}10^4$	$1.80{\cdot}10^4$	$1.80{\cdot}10^4$	$1.78{\cdot}10^4$	$1.70{\cdot}10^4$	$1.58{\cdot}10^4$	$1.49{\cdot}10^4$	$1.49{\cdot}10^4$	$2.12{\cdot}10^4$
density (g/cm^3)	0.97	1.18	1.18	1.19	1.04	1.21	1.41	1.38	1.03

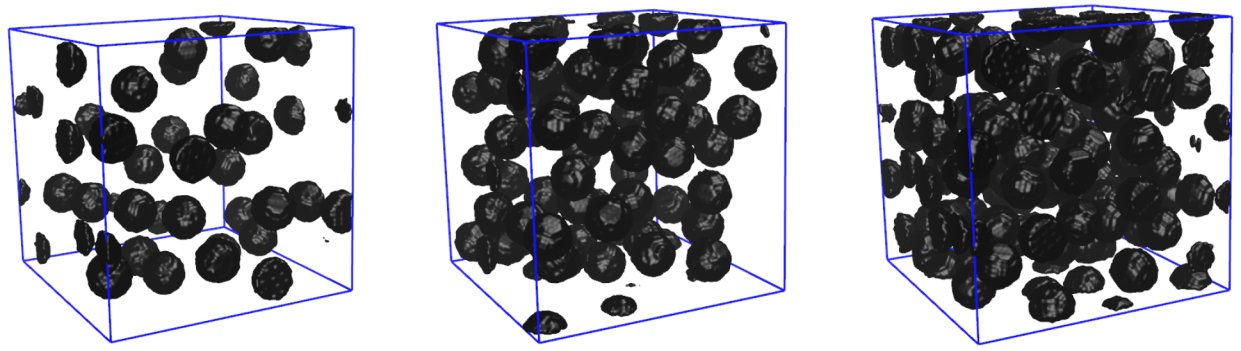

Figure 3. Snapshots of systems with varying NP concentrations. From left to right: 6, 14, and 20% by volume.

System Assembly

Following the above procedure, we generated nine simulation boxes with different grafting densities, NP concentrations, and cross-link (CL) densities. Accordingly, we shall refer to each system by the following shorthand notation: [grafting coverage (bonds/nm^2), NP concentration (vol %), CL density (SS/chain)]. Table 3 summarizes their constitution and their main structural properties.

The largest value of the grafting density (0.56 nm^{-2}) corresponds to the situations in which 100% of the linkers' terminals were chemically bonded to the polymer. With these as a starting point, other systems with a lower grafting density were generated by simply deleting a suitable fraction of bonds.

The volume fraction (ϕ_{NP}) of silica was varied between 0 and 20%. The NPs were arranged so to obtain nonoverlapping, well-separated distributions. The overall filler content corresponds to a loading of 59 phr or lower. The phr units are commonly used in rubber formulations, and they stand for "per hundred rubber".[4] A loading of 59 phr corresponds to a blend of m_{NP} = 59 g (mass of nanoparticles) and m_{PB} = 100 g (mass of rubber). The conversion to volume fraction is obtained as

$$\phi_{NP} = \frac{V_{NP}}{V_{NP} + V_{PB}} \times 100 = \frac{m_{NP}\rho_{PB}}{m_{NP}\rho_{PB} + m_{PB}\rho_{NP}} \times 100 \quad (6)$$

where V_{NP} and V_{PB} are the volumes of each phase, and we have assumed that these are additive. The second expression involves the densities, which can be taken as equal to ρ_{PB} = 0.93 g/cm^3 for polybutadiene and ρ_{NP} = 2.2 g/cm^3 for silica.[68] Figure 3 shows three examples of systems with increasing NP loadings. The overall number of NPs is given in Table 3.

The CL densities used in this work were in the range of 1.2−2.0 S−S precursors per PB chain, similar to that in our previous work.[46] This corresponds to 1.4−2.4 phr of sulfur, comparable to the amounts employed in typical rubber formulations.[4] According to our earlier investigation,[46] a fully developed three-dimensional network is obtained in an unfilled system with the higher sulfur concentration (i.e., the systems are well above the percolation threshold), while the lower concentration may leave a small number of chains unconnected to the rest of the network. Note, however, that in a filled network the NPs effectively act as additional cross-linking points of high functionality, thanks to the bonds formed by the silane coupling agents.

Simulation Protocol

The average number of coarse-gained atoms or beads in our systems was about 6 × 10^5 (see Table 3). Throughout our simulations, the temperature was set at 298 K and the pressure at 1 atm, unless stated otherwise. The MD equations of motion were integrated with a 2 fs time step (a conservative choice, for a united-atom force field).

The initial cubic box dimension was set so as to produce a density of 0.93 g/cm^3 in the space accessible to the polymer (i.e., excluding the volume of the NPs). Prior to cross-linking, initial equilibration of the rubber matrix was performed in the NVT ensemble, keeping the NPs at fixed positions. A soft pair potential was used at this stage, so to allow the polymer chains to uniformly distribute around and outside the NPs, bypassing their mutual entanglements.[69] After 4 ns, the Lennard−Jones interactions were introduced, replacing the soft potentials. The system was then further equilibrated for 20 ns in the NPT ensemble. Cross-linking of the polymers and formation of the chemical bonds between the silane linkers and the polymer chains were performed simultaneously after this volume relaxation, by a stepwise reaction−relaxation procedure analogous to that described in our previous work.[46] In particular, we performed 40 cycles of bond formation and stiffening, each lasting 4 ns, followed by a final NPT equilibration of 2 ns. This strategy avoids the rapid, possibly catastrophic buildup of local stresses within the matrix, following formation of new chemical bonds. This problem may occur also for coarse-grained bead-and-spring models, but it is especially severe for atomistic models, due to the large mismatch between the van der Waals and the covalent radii of the elements (the bonds are always highly stretched when they are formed). The final densities were within the expected range, although with some exceptions, plausibly related to the difficulty of achieving a full volume relaxation in the systems with the higher degrees of filler loading and cross-linking (see Table 3).

Nonequilibrium molecular dynamics (NEMD) simulations of the deformation were based on the SLLOD algorithm for elongational flow,[29,70] as described and tested in our previous work.[46] Box elongation followed the equation $\lambda(t) = 1 + rt$, with a rate r = 1.0 ns^{-1}, where $\lambda(t) = L_x(t)/L_x(0)$ is the ratio of deformed and initial box sizes along the stretching direction, respectively. Deformation in the two orthogonal directions was equal to $\lambda(t)^{-1/2}$, under the reasonable assumption (for rubber) that deformation occurs at constant volume.

https://doi.org/10.1021/acspolymersau.1c00023
ACS Polym. Au 2021, 1, 175−186

Table 4. Mechanical Properties of the Simulated Systems

	[grafting coverage (nm^{-2}), NP concentration (vol %), CL density (SS/chain)]								
	[0, 0, 2]	[0, 20, 2]	[0.14, 20, 2]	[0.56, 20, 2]	[0.56, 6, 2]	[0.56, 14, 2]	[0.56, 20, 1.6]	[0.56, 20, 1.2]	[0.14, 6, 1.6]
Young's modulus (MPa)	24.6	30.2	29.7	69.2	34.9	52.6	61.5	54.9	24.1
elongation at first broken bond	3.7	3.3	3.3	1.4	1.8	1.5	1.5	1.5	4.2
elongation at failure (λ^*)	5.7	5.9	5.9	4.3	5.9	4.4	5.5	5.0	6.3
stress at failure (MPa)	973.0	1038.0	1043.0	964.0	1117.0	992.0	1141.0	846.0	757.0
work of fracture (MPa)	799.0	728.0	788.0	788.0	902.0	750.0	935.0	734.0	619.0
void volume at failure (nm^3)	392.0	370.0	327.0	430.0	578.0	189.0	393.0	889.0	1286.0
void fraction at failure (%)	2.99	2.57	2.27	3.03	3.61	1.39	3.30	7.47	8.04
voids at failure (count)	10	80	85	39	35	24	18	2	9
av void radius at failure (nm)	4.0	12.9	12.0	8.5	22.1	19.6	12.6	13.8	27.1

RESULTS AND DISCUSSION

Table 4 collects the main quantitative descriptors of the mechanical properties of the simulated systems. The following pages are largely devoted to the discussion of these quantities and their interpretation. We state from the outset that, given the approximations in our models and the limited range of time scales accessible by MD simulations, one cannot presently expect more than a qualitative agreement with experiments on filled rubbers. In particular, due to the high deformation rate, the stress values may be up to 1 order of magnitude larger than typical experimental values.[46] Nonetheless, to balance their limitations, MD simulations have the distinctive advantage of offering a detailed atomistic view of the processes occurring in these materials as they deform and break.

Stress–Strain Curves

In Figure 4 we compare the stress–strain curves of the unfilled networks (ϕ_{NP} = 0%) with harmonic (unbreakable) and Morse (breakable) bond potentials, respectively. Note that the stress output by LAMMPS and reported here is the σ_{zz} component of the "true stress", which corresponds to the ratio of the pulling force and the deformed sample cross-section (unlike the "engineering stress", where the force is divided by the undeformed cross-section). The two curves appear to be almost perfectly superposable up to λ = 3. Above this value, the harmonic potential leads a parabolic increase of the stress with the applied strain. Instead, the Morse potential initially produces a slower decrease and then, from λ = 5 up to λ = 7, there is a broad plateau where the network undergoes progressive, irreversible damage (see below). Upon further deformation, the stress decreases markedly, eventually leading to a complete breakup of the rubber sample at λ > 11. Below we shall look at mechanisms underlying these curves in greater detail.

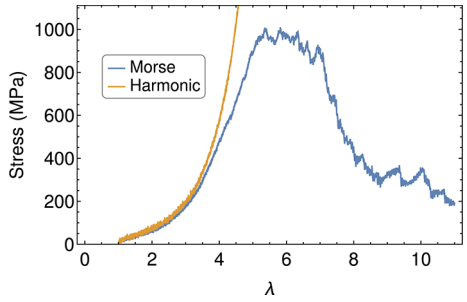

Figure 4. Comparison between the stress–strain curves of the unfilled network with harmonic and Morse bond potentials.

Having tested the suitability of the Morse potentials for describing the mechanics of network deformation and fracture, we examine the relationship between the composition and stress–strain response of the systems. Figures 5–7 show the effects associated with a change of the grafting densities, the amount of cross-linking, and the silica volume fraction, respectively. The main mechanical descriptors, each normalized by the highest value in each series, are shown in the right-hand panels of each figure. This allows a direct visualization of the effect of a particular variable on the mechanical properties. In general, in order to compare different systems, we conventionally identify the "failure condition" with the first maximum of the stress–strain curves. The elongation (λ^*) and the stress at this point are reported in Table 4. Several other quantities in the table are calculated at this point. As we shall see, the first maximum of the stress is preceded by several yield events, which we identify with the breaking of chemical bonds. It is eventually followed by complete fracture of the samples, when the stress

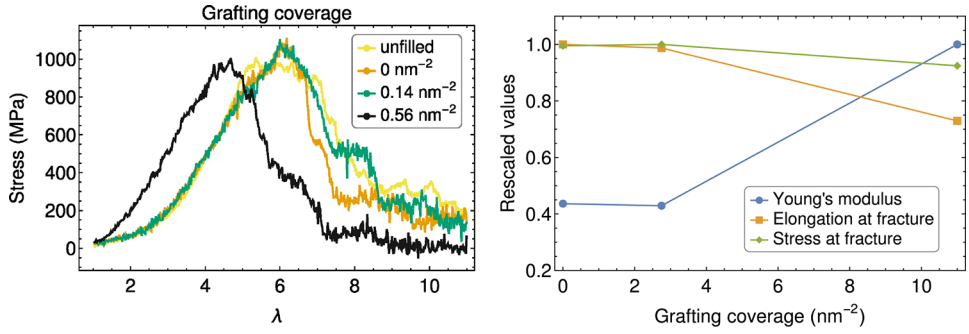

Figure 5. Stress–strain profiles (left) and normalized mechanical properties (right) for systems with varying degrees of grafting coverage. The CL density is 2.0 SS/chain, and the NP volume fraction is 20%. The unfilled network is also included, for comparison.

https://doi.org/10.1021/acspolymersau.1c00023
ACS Polym. Au 2021, 1, 175–186

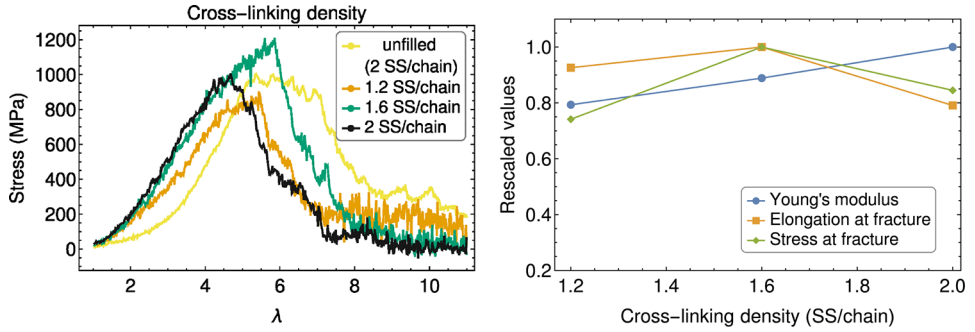

Figure 6. Stress−strain profiles (left) and normalized mechanical properties (right) for systems with varying cross-linking densities. The grafting coverage is 0.56 nm^{-2}, and the NP volume fraction is 20%. The unfilled network is also included, for comparison.

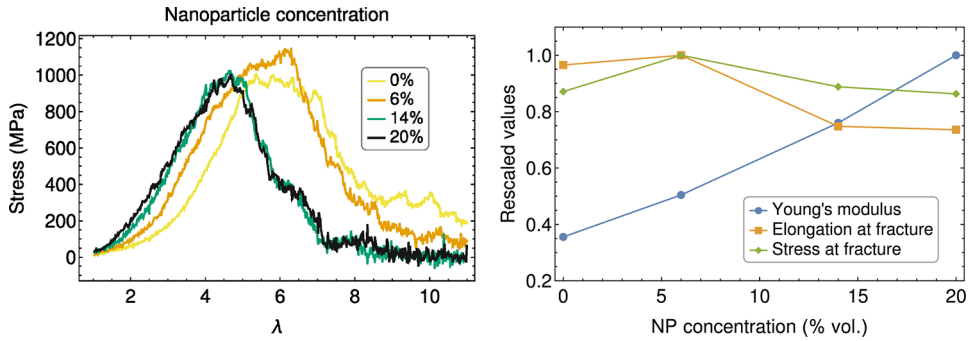

Figure 7. Stress−strain profiles (left) and normalized mechanical properties (right) for systems with varying NP volume fractions. The grafting coverage is 0.56 nm^{-2}, and the CL density is 2.0 SS/chain. The unfilled network is also included, for comparison.

goes to zero. The work of fracture is calculated as the integral of the stress−strain curve over the $\lambda = 1-10$ range. It is reported in MPa, as it has the dimension of a stress (or an energy per unit volume). The Young modulus is obtained by linear fits of the stress−strain curves up to $\lambda = 2.0$, well before the onset of damage.

Changes in grafting coverage (Figure 5) seem to affect mainly the stiffness and elongation at fracture. The densely grafted system (0.56 nm^{-2}) is characterized by a significant increase in the Young modulus, but with a drop in the stress and elongation after the maximum. Also, fracture in this system appears to be complete around $\lambda = 9$ (the stress is essentially zero, excluding thermal fluctuations), while the less grafted systems do not break completely before $\lambda = 11$, as for the unfilled network. Composites with bare and lightly grafted NPs show similar mechanical properties, only slightly above those observed in the unfilled rubber matrix. However, the presence of shoulders beyond the maximum suggest a more gradual fracture process. This is especially true for the system with a low grafting density, at 0.14 nm^{-2}. Interestingly, the overall value of the work of fracture (integral of the curves) is relatively insensitive to these changes in the interfacial bonding.

Increasing CL density (Figure 6) produced a linear increase in the Young modulus of the composites, as expected from fundamental theories of rubber elasticity[9] and in agreement with our previous simulations of the unfilled networks. Instead, the elongation and stress at failure depend in a nonmonotonic way on this variable. The system with the best performance, combining a relatively large modulus at small deformation and increased resistance to fracture, had a cross-linking density of 1.6 SS/chain. Unfortunately, this was also characterized by an abrupt drop in stress right after the maximum. Despite this, this particular system was characterized by the largest overall value of the work of fracture.

A similar outcome was observed on changing the NP concentration (Figure 7). The Young modulus appears to increase more than linearly with the filler volume fraction, in agreement with hydrodynamic models of reinforcement.[14,15,71] The maximum values of both strain and stress at failure occur at a relatively small volume fraction: namely, ϕ_{NP} = 6%. This system has the second largest work of fracture, after that with ϕ_{NP} = 20% but a lower CL density (see above). Also here, however, the stress decays more quickly than in the unfilled system beyond the maximum. This suggests that the NPs produce a mechanical reinforcement at small deformations but ultimately lead to a more fragile system, prone to premature fracture. This conclusion may also depend on the high rates of deformation that are used in our simulations. Note that mechanical reinforcement could also be expected to depend non-monotonically on the degree of particle dispersion, being maximum when the NPs form tenuous fractal aggregates spanning the whole sample volume.[2,71] However, dispersion could not be considered a variable in this work, since we only simulated well-dispersed morphologies with little or no interparticle contacts.

On the basis of the top-performing parameters extracted from our simulations, we assembled the test system identified as [0.14, 6, 1.6]. Its simulated stress−strain curve is shown in Figure 8, alongside that of the unfilled network. The results are somewhat disappointing from the point of view of the mechanical descriptors in Table 4, especially due to the slight lowering of the modulus and the marked decrease in the stress at the failure point. On the positive side, there is now a prominent shoulder in the stress−strain curve after this maximum, indicating that the system has a certain toughness, by which

https://doi.org/10.1021/acspolymersau.1c00023
ACS Polym. Au 2021, 1, 175−186

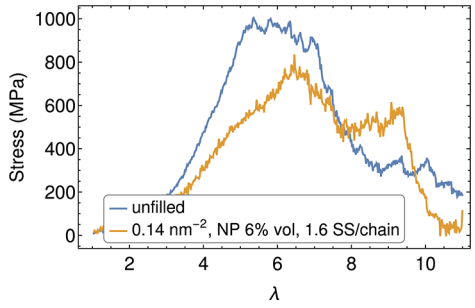

Figure 8. Stress−strain curve of the "optimal" system.

we mean the capacity to resist an abrupt, catastrophic fracture. The stress drop associated with the disruption of the network appears much less pronounced than in the other simulations, and the shoulder at $\lambda = 9.6$, already present in the [0.14, 20, 2] system, seems to be enhanced. Overall, this attempt demonstrates that the simultaneous introduction of the "optimal" ingredients may not lead to a straightforward improvement in the mechanical properties. It is a clear demonstration of the strong coupling between the variables defining the composition and the structure of polymer networks and nanocomposites. Further work will be necessary in order to clarify this issue.

Bond Cleavage and Connectivity

Having assessed the mechanical properties of the model PNCs, we now seek a microscopic interpretation of our observations. The failure and fracture of materials are the macroscopic manifestations of many molecular-level events, when their number and spatial extent overcome certain critical values. The breaking of a chemical bond is the simplest, most easily identified event of this sort. Understanding the mechanics of bond breaking is important also because it is an important energy dissipation mechanism, which can be harnessed to produce tougher networks and gels.[9,13]

Figure 9 summarizes our findings on the strain-induced breaking of chemical bonds. In most of our simulations, the first cleavage events involve the S−S bonds of the silane linkers, at the interface between the particles and the rubber matrix. Subsequently, fracture develops inside the matrix by breaking the S−S bonds connecting the chains and ultimately the CH_2−CH_2 bonds within the chains. All of the other non-Si−Si or non-Si−CH_2 bonds can break, but they do so in very small numbers.

The S−S bonds start to break well before the failure points (vertical dashed lines in Figure 9), which we have identified with the first maxima in the stress. The fact that S−S bonds are the weakest links in our networks correlates with their low dissociation energies (see the D values in Table 2). The fact that the interfacial S−S bonds break before those in the bulk is most likely a consequence of stress concentration effects, which develop within a strongly heterogeneous material upon deformation. To some extent, the differences between the curves for one or the other type of S−S bond depend also on their relative numbers. In systems where the NP concentration or grafting coverage is low, the curve describing the breakup of matrix S−S bonds lies higher than the interfacial S−S curve, simply because there are very few bonds of the latter type in the starting structure.

The bond-breaking analysis finds an experimental counterpart in the work by Clough et al.,[72] in which the breaking of bonds during the deformation of a rubber nanocomposite was visualized and quantified with mechanoluminescent probes. This work confirmed the connection between the premature rupture of bonds during the first deformation cycle and the Mullins effect, a nonreversible softening of the material at moderate to large deformations.[73] Here we have performed a linear, noncyclic deformation; therefore, we cannot investigate the hysteresis in the stress−strain curves caused by the Mullins effect. However, we do observe premature bond breakage, well before the formation of voids (see "elongation at first broken bond" in Table 4).

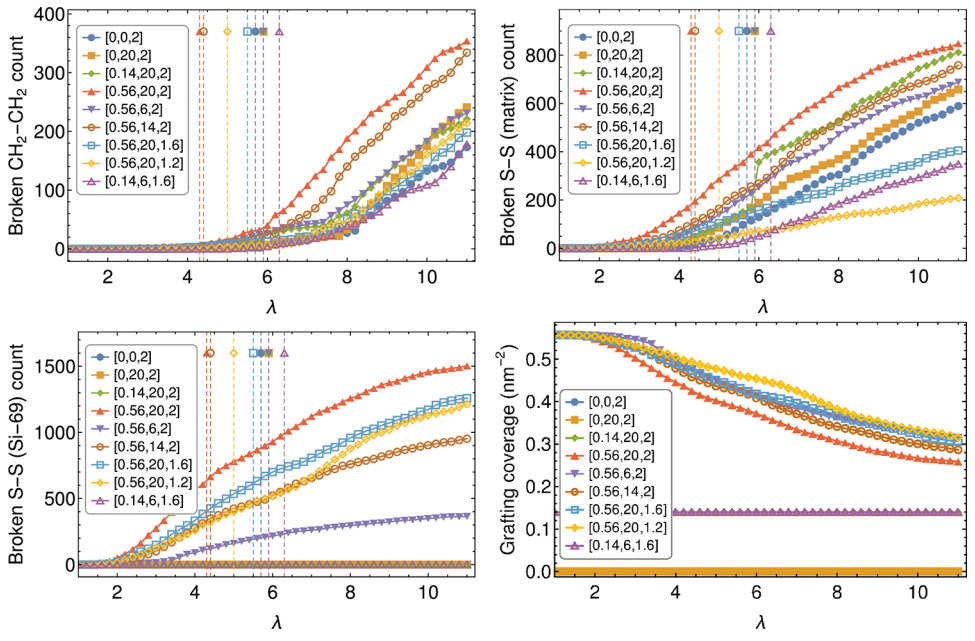

Figure 9. Broken bond counts for (a) CH_2−CH_2, (b) S−S in the matrix, and (c) S−S of the silane linkers. (d) Strain dependence of the average grafting coverage. λ^* values are reported with vertical dashed lines pinned with the corresponding symbol.

https://doi.org/10.1021/acspolymersau.1c00023
ACS Polym. Au 2021, 1, 175−186

Systems with low grafting coverage are characterized by a delayed occurrence of bond rupture. This is not strictly related to larger elongation at break; in fact, the system [0.56, 6, 2] presents late fracture and dense grafting (see Figure 7). It can be argued that, if the grafting coverage is excessively high, the system responds to deformation by first breaking some grafting links. By lowering the amount of covalent bonding between the NPs and the matrix, the system releases stress and dissipates mechanical energy.

The evolution of the average grafting density throughout the deformation gives information complementary to the number of broken S−S bonds of the Si-69 linkers. The fourth panel in Figure 9 shows that systems with same initial grafting density have a similar evolution, despite differences in the NP concentration or CL density.

Figure 10 shows the existence of a linear correlation between the elongation at failure and the average rate of bond breaking,

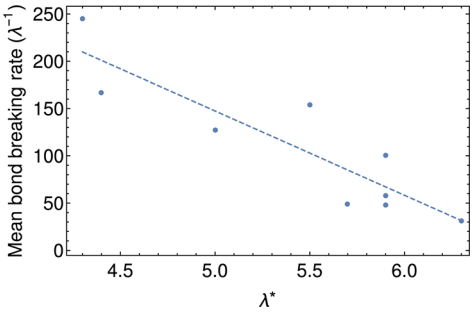

Figure 10. Scatter plot and linear fit of the average bond-breaking rate versus the deformation at failure λ^*.

calculated as the average slope of the curves in Figure 9. In systems where the bond-breaking rate is higher, we generally observe a premature maximum in the stress. This proves the relationship between the mechanical or macroscopic view of fracture and the chemical or microscopic perspective. Instead, we have found no clear correlation between the change in slope of the bond-breaking curves and the stress−strain curves, especially with the occurrence of the drop of stress. Our attempt to interpret this part of the stress−strain curves will be discussed in the next section.

Void Formation

From a continuum mechanics perspective, fracture is connected to the formation and growth of cracks and voids. These must arise from bond breaking, but on a larger length scale. The very concept of a void, which is natural and almost requires no definition in a macroscopic context, becomes somewhat uncertain at the molecular level. One common way of detecting voids in molecular models is based on building an occupancy grid. Here we have used an approximate but effective way of keeping track of the formation and evolution of voids, exploiting the VORO++ package[74] within LAMMPS to perform a Voronoi analysis. The Voronoi tessellation produces a partitioning of the total simulated volume, by assigning a portion of it to each atom. A Voronoi cell, which by construction contains a single atom, was considered to be "void" if its volume was greater than 100 Å^3. Polyhedral cells that exceed this value and share a face are first neighbors, and they are considered to be part of the same void. Figure 11 illustrates the process of void identification using a 2D representation.

Figure 12 shows the snapshots of the systems at their failure point, corresponding to the λ^* elongation. Different colors are used for distinct voids. The quantitative data on the volume, dimension, and number of voids are reported in Table 4. Note that, in order to compare systems with different NP loadings, the "volume fraction at failure" has been obtained by dividing the total void volume by the volume of the polymer matrix.

It is interesting to compare the effects of lowering the cross-links in the matrix or the bonds at the boundary between the NP and the matrix. Although in the analyzed concentration range both actions lead to a larger elongation at failure, the first action results in fewer larger voids, while the second produces more, smaller voids. Indeed, a lower CL density within the matrix allows large sliding among the chains and facilitates the formation of macro-voids in the matrix. Large voids are also observed in the unfilled matrix, and in fact there is a tendency to form larger voids by lowering the NP concentration. Instead, by lowering the density of grafting bonds, many small voids nucleate at the NP surfaces.

Although the number and dimension of voids are different among the analyzed systems, the evolution of the voids during the deformation are analogous. Figure 13 demonstrates this for two systems that qualitatively appear to be very different.

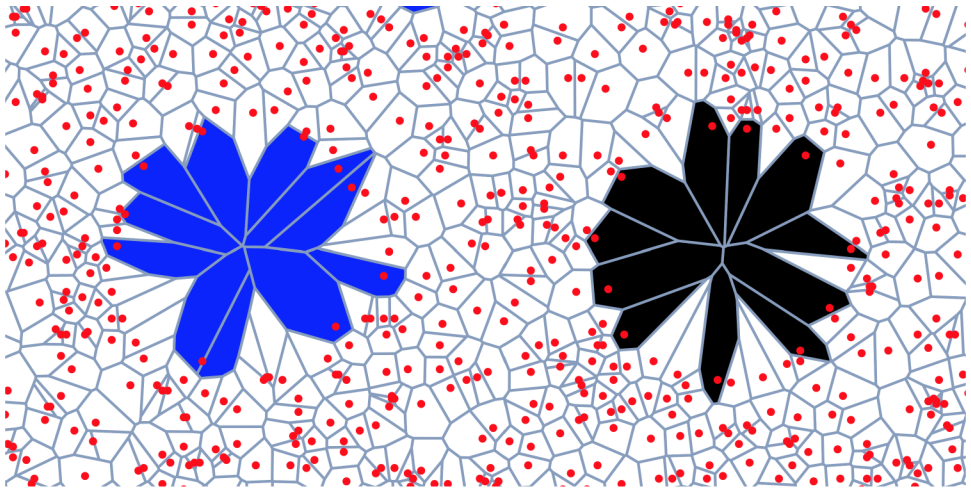

Figure 11. Diagram showing a Voronoi tessellation of a 2D random distribution of points characterized by two differently colored macro-voids. The areas that have extension exceeding a threshold value are considered voids. The neighboring voids are considered part of the same macro-void.

https://doi.org/10.1021/acspolymersau.1c00023
ACS Polym. Au 2021, 1, 175−186

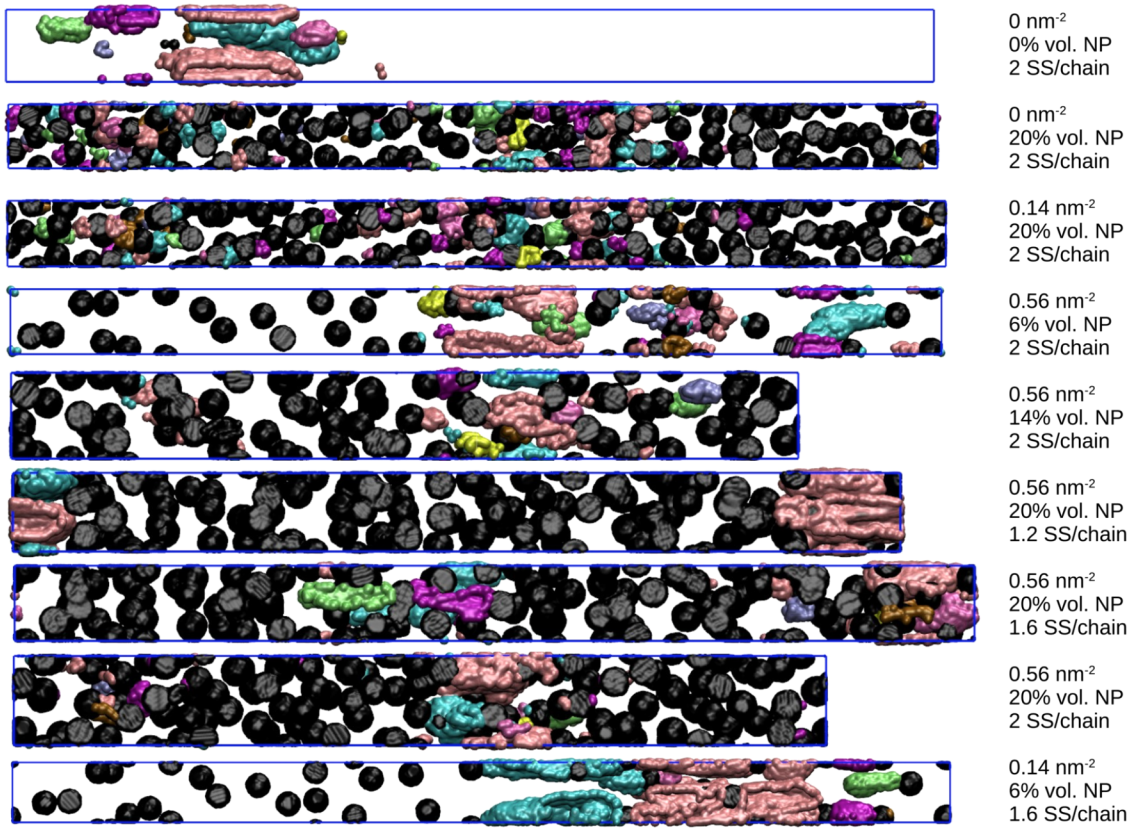

Figure 12. Snapshots of the systems at λ^*. Individual voids are colored differently and represented using isodensity surfaces. NPs are reported in black, using the same method.

Indeed, the system [0, 20, 2] shows numerous small voids, while the system [0.14, 6, 1.6] has few larger voids. The chart bars show that in both cases fracture initiates with some small voids, which grow in number until the λ^* elongation and then coalesce to a few macro-voids. In comparison to bond scission, the formation of voids seems to have a closer connection with the overall shape of the stress−strain curve. The void histograms clarify that the first drop in the curve (at λ^*) happens when the voids reach the maximum number and start to coalesce.

CONCLUSIONS

We have performed and presented large-scale, near-atomistic simulations of the elasticity and fracture of silica-filled polybutadiene networks. We have explored the influence of grafting, cross-linking, and nanoparticle concentration on the mechanical properties of the nanocomposites and analyzed the results in terms of bond-breaking events as well as the formation and evolution of voids within the rubber matrix. For the sake of computational efficiency, due to the large size of our systems, we have been forced to employ very high deformation rates (1 ns^{-1}). For this reason, the results presented here should be confirmed using much lower deformation rates (at least by 1 order of magnitude) and possibly different nonequilibrium MD algorithms, using adequate computational resources. Nonetheless, for the time being, the qualitative conclusions appear to be reasonable. In particular, the systems' response is definitely rubber-like. Thus, even though we have mostly focused on the failure of the networks, it is noteworthy that these can be stretched up to 100−200% of their original length with little or no apparent damage, such as bond breaking. More realistic simulations should also include somewhat larger particles and longer precursor chains, following for example the approach of Caputo et al.[75] to equilibrate the systems.

We have found that the influence of the cross-link and nanoparticle concentrations on the stiffness of the materials is strictly monotonic, as expected, while the effect of the grafting density at the polymer−nanoparticle interface is more subtle. This may partially explain the contrasting results obtained by other authors in a series of earlier works.[76−78] A complex dependence was found also for the stress and elongation at fracture, which are known to be particularly hard to improve, even experimentally. The overall picture agrees with coarse-grained simulation results by Hagita et al.,[35] especially on the mechanisms of formation, growth, and coalescence of void within the network. In particular, we have observed that the increase in grafting density is responsible for the formation of numerous small voids at the boundary between the surface and the matrix, and the increase in cross-linking density prevents the formation of larger voids inside the matrix.

The present work is based on previous publications by our group for the parametrization of a coarse-grained silica model compatible with the united-atom model for polybutadiene[45] and the development of strategies to simulate the cross-linking reaction and probe the mechanical properties of the resulting networks.[46] In the future, we hope to pursue this research program by further improvements in the models (e.g., reactive force fields), of the simulation algorithms (e.g., other non-equilibrium methods and eventually multiscale coupling to finite-element simulations[79]), in the data analysis (e.g., evaluation of local strains and stresses, identification of energy dissipation mechanisms), and more generally in the bottom-up

https://doi.org/10.1021/acspolymersau.1c00023
ACS Polym. Au 2021, 1, 175−186

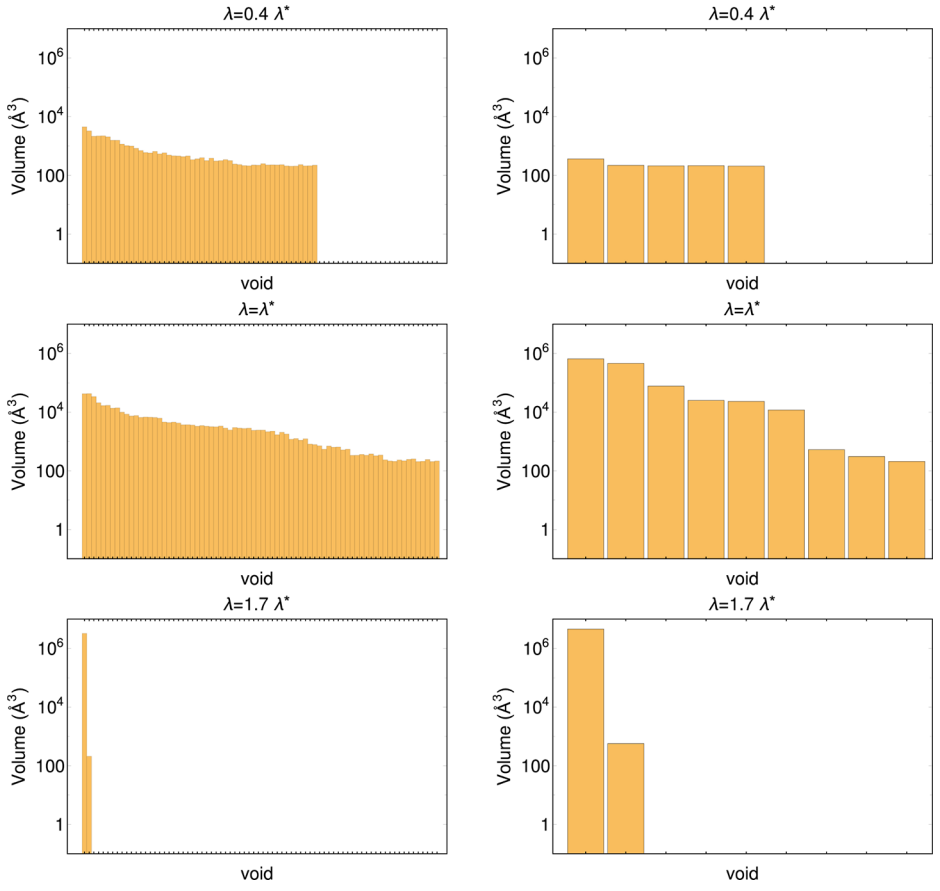

Figure 13. Bar charts of the volume of each void formed at three stages of deformation, for the [0, 20, 2] system (left) and the [0.14, 6, 1.6] system (right).

design of soft nanocomposites (e.g., systematic exploration of variables and optimization of properties).

AUTHOR INFORMATION

Corresponding Author

Guido Raos − *Department of Chemistry, Materials and Chemical Engineering, "G. Natta", Politecnico di Milano, Milano 20131, Italy;* orcid.org/0000-0001-7011-4036; Email: guido.raos@polimi.it

Authors

Alessio David − *Department of Chemistry, Materials and Chemical Engineering, "G. Natta", Politecnico di Milano, Milano 20131, Italy*

Ugo Tartaglino − *Pirelli Tyre S.p.A., 20126 Milano, Italy*

Mosè Casalegno − *Department of Chemistry, Materials and Chemical Engineering, "G. Natta", Politecnico di Milano, Milano 20131, Italy;* orcid.org/0000-0002-4833-2990

Complete contact information is available at: https://pubs.acs.org/10.1021/acspolymersau.1c00023

Notes

The authors declare no competing financial interest.

ACKNOWLEDGMENTS

This research was funded by Pirelli Tyre S.p.A. and Fondazione Politecnico di Milano under the Pirelli Politecnico di Milano Joint Labs framework.

REFERENCES

(1) Kumar, S. K.; Benicewicz, B. C.; Vaia, R. A.; Winey, K. I. 50th anniversary perspective: are polymer nanocomposites practical for applications? *Macromolecules* **2017**, *50*, 714−731.

(2) Jancar, J.; Douglas, J.; Starr, F.; Kumar, S.; Cassagnau, P.; Lesser, A.; Sternstein, S.; Buehler, M. Current issues in research on structure−property relationships in polymer nanocomposites. *Polymer* **2010**, *51*, 3321−3343.

(3) Vilgis, T. A.; Heinrich, G.; Klüppel, M. *Reinforcement of Polymer Nano-Composites: Theory, Experiments and Applications*; Cambridge University Press: 2009.

(4) Gent, A. N. *Engineering with Rubber. How to Design Rubber Components*; Hanser: 2012.

(5) Erman, B.; Mark, J. E. *Structures and properties of rubberlike networks*; Oxford University Press: 1997.

(6) Weiner, J. H. *Statistical mechanics of elasticity*; Dover Publications: 2012.

(7) Ronca, G.; Allegra, G. An approach to rubber elasticity with internal constraints. *J. Chem. Phys.* **1975**, *63*, 4990−4997.

(8) Rubinstein, M.; Panyukov, S. Elasticity of Polymer Networks. *Macromolecules* **2002**, *35*, 6670−6686.

(9) Danielsen, S. P. O.; et al. Molecular Characterization of Polymer Networks. *Chem. Rev.* **2021**, *121*, 5042−5092.

(10) Grest, G. S.; Kremer, K. Statistical properties of random cross-linked rubbers. *Macromolecules* **1990**, *23*, 4994−5000.

(11) Everaers, R.; Sukumaran, S. K.; Grest, G. S.; Svaneborg, C.; Sivasubramanian, A.; Kremer, K. Rheology and microscopic topology of entangled polymeric liquids. *Science* **2004**, *303*, 823−826.

(12) Jha, K. C.; Tsige, M. MOLECULAR MODELING OF THERMAL AND MECHANICAL PROPERTIES OF ELASTOMERS: A REVIEW. *Rubber Chem. Technol.* **2013**, *86*, 401−422.

(13) Creton, C. 50th Anniversary Perspective: Networks and Gels: Soft but Dynamic and Tough. *Macromolecules* **2017**, *50*, 8297−8316.
(14) Allegra, G.; Raos, G.; Vacatello, M. Theories and simulations of polymer-based nanocomposites: From chain statistics to reinforcement. *Prog. Polym. Sci.* **2008**, *33*, 683−731.
(15) Christensen, R. M. *Mechanics of composite materials*; Dover Publications: 2005.
(16) Rittigstein, P.; Priestley, R. D.; Broadbelt, L. J.; Torkelson, J. M. Model polymer nanocomposites provide an understanding of confinement effects in real nanocomposites. *Nat. Mater.* **2007**, *6*, 278−282.
(17) Papon, A.; Montes, H.; Lequeux, F.; Oberdisse, J.; Saalwächter, K.; Guy, L. Solid particles in an elastomer matrix: impact of colloid dispersion and polymer mobility modification on the mechanical properties. *Soft Matter* **2012**, *8*, 4090.
(18) Song, Y.; Zheng, Q. Concepts and conflicts in nanoparticles reinforcement to polymers beyond hydrodynamics. *Prog. Mater. Sci.* **2016**, *84*, 1−58.
(19) Cheng, S.; Carroll, B.; Bocharova, V.; Carrillo, J.-M.; Sumpter, B. G.; Sokolov, A. P. Focus: Structure and dynamics of the interfacial layer in polymer nanocomposites with attractive interactions. *J. Chem. Phys.* **2017**, *146*, 203201.
(20) Harito, C.; Bavykin, D. V.; Yuliarto, B.; Dipojono, H. K.; Walsh, F. C. Polymer nanocomposites having a high filler content: synthesis, structures, properties, and applications. *Nanoscale* **2019**, *11*, 4653−4682.
(21) Zuo, B.; Zhou, H.; Davis, M. J.; Wang, X.; Priestley, R. D. Effect of Local Chain Conformation in Adsorbed Nanolayers on Confined Polymer Molecular Mobility. *Phys. Rev. Lett.* **2019**, *122*, 217801.
(22) Hanakata, P. Z.; Pazmino Betancourt, B. A.; Douglas, J. F.; Starr, F. W. A unifying framework to quantify the effects of substrate interactions, stiffness, and roughness on the dynamics of thin supported polymer films. *J. Chem. Phys.* **2015**, *142*, 234907.
(23) Pastore, R.; David, A.; Casalegno, M.; Greco, F.; Raos, G. Influence of wall heterogeneity on nanoscopically confined polymers. *Phys. Chem. Chem. Phys.* **2019**, *21*, 772−779.
(24) Baggioli, A.; Casalegno, M.; David, A.; Pasquini, M.; Raos, G. Polymer-Mediated Adhesion: Nanoscale Surface Morphology and Failure Mechanisms. *Macromolecules* **2021**, *54*, 195−202.
(25) Giunta, G.; Chiricotto, M.; Jackson, I.; Karimi-Varzaneh, H. A.; Carbone, P. Multiscale modelling of heterogeneous fillers in polymer composites: The case of polyisoprene and carbon black. *J. Phys.: Condens. Matter* **2021**, *33*, 194003.
(26) Liu, J.; Zhang, L.; Cao, D.; Shen, J.; Gao, Y. COMPUTATIONAL SIMULATION OF ELASTOMER NANOCOMPOSITES: CURRENT PROGRESS AND FUTURE CHALLENGES. *Rubber Chem. Technol.* **2012**, *85*, 450−481.
(27) Karatrantos, A.; Clarke, N.; Kröger, M. Modeling of Polymer Structure and Conformations in Polymer Nanocomposites from Atomistic to Mesoscale: A Review. *Polym. Rev.* **2016**, *56*, 385−428.
(28) Gartner, T. E.; Jayaraman, A. Modeling and Simulations of Polymers: A Roadmap. *Macromolecules* **2019**, *52*, 755−786.
(29) Allen, M. P.; Tildesley, D. J. *Computer simulation of liquids*; Oxford University Press: 2017.
(30) Raos, G.; Moreno, M.; Elli, S. Computational Experiments on Filled Rubber Viscoelasticity: What Is the Role of Particle-Particle Interactions? *Macromolecules* **2006**, *39*, 6744−6751.
(31) Raos, G.; Casalegno, M. Nonequilibrium simulations of filled polymer networks: Searching for the origins of reinforcement and nonlinearity. *J. Chem. Phys.* **2011**, *134*, 054902.
(32) Gavrilov, A. A.; Chertovich, A. V.; Khalatur, P. G.; Khokhlov, A. R. Study of the Mechanisms of Filler Reinforcement in Elastomer Nanocomposites. *Macromolecules* **2014**, *47*, 5400−5408.
(33) Goyal, S.; Escobedo, F. A. Structure and transport properties of polymer grafted nanoparticles. *J. Chem. Phys.* **2011**, *135*, 184902.
(34) Hagita, K.; Morita, H.; Doi, M.; Takano, H. Coarse-Grained Molecular Dynamics Simulation of Filled Polymer Nanocomposites under Uniaxial Elongation. *Macromolecules* **2016**, *49*, 1972−1983.
(35) Hagita, K.; Morita, H.; Takano, H. Molecular dynamics simulation study of a fracture of filler-filled polymer nanocomposites. *Polymer* **2016**, *99*, 368−375.
(36) Xiao, S.; Peter, C.; Kremer, K. Systematic comparison of model polymer nanocomposite mechanics. *Bioinspiration and Biomimetics* **2016**, *11*, 055008.
(37) Davris, T.; Mermet-Guyennet, M. R. B.; Bonn, D.; Lyulin, A. V. Filler Size Effects on Reinforcement in Elastomer-Based Nanocomposites: Experimental and Simulational Insights into Physical Mechanisms. *Macromolecules* **2016**, *49*, 7077−7087.
(38) Molinari, N.; Sutton, A.; Mostofi, A. Mechanisms of reinforcement in polymer nanocomposites. *Phys. Chem. Chem. Phys.* **2018**, *20*, 23085−23094.
(39) Pasquini, M.; Raos, G. Tunable interaction potentials and morphology of polymer−nanoparticle blends. *J. Chem. Phys.* **2020**, *152*, 174902.
(40) Pavlov, A. S.; Khalatur, P. G. Fully atomistic molecular dynamics simulation of nanosilica-filled crosslinked polybutadiene. *Chem. Phys. Lett.* **2016**, *653*, 90−95.
(41) Meyer, J.; Hentschke, R.; Hager, J.; Hojdis, N. W.; Karimi-Varzaneh, H. A. Molecular Simulation of Viscous Dissipation due to Cyclic Deformation of a Silica−Silica Contact in Filled Rubber. *Macromolecules* **2017**, *50*, 6679−6689.
(42) Yuan, B.; Zeng, F.; Peng, C.; Wang, Y. Coarse-grained molecular dynamics simulation of cis-1,4-polyisoprene with silica nanoparticles under extreme uniaxial tension. *Modell. Simul. Mater. Sci. Eng.* **2021**, *29*, 055013.
(43) Ozawa, Y.; Takata, T. Synthesis and property of end-functionalized poly(cis-1,4-butadiene) and its application to rubber compound. *J. Appl. Polym. Sci.* **2019**, *136*, 47985.
(44) Zhu, Z.; Thompson, T.; Wang, S.-q.; von Meerwall, E. D.; Halasa, A. Investigating Linear and Nonlinear Viscoelastic Behavior Using Model Silica-Particle-Filled Polybutadiene. *Macromolecules* **2005**, *38*, 8816−8824.
(45) David, A.; Pasquini, M.; Tartaglino, U.; Raos, G. A Coarse-Grained Force Field for Silica−Polybutadiene Interfaces and Nanocomposites. *Polymers* **2020**, *12*, 1484.
(46) David, A.; Tartaglino, U.; Raos, G. Towards realistic simulations of polymer networks: tuning vulcanisation and mechanical properties. *Phys. Chem. Chem. Phys.* **2021**, *23*, 3496−3510.
(47) Buehler, M. J.; Keten, S. Colloquium: Failure of molecules, bones, and the Earth itself. *Rev. Mod. Phys.* **2010**, *82*, 1459−1487.
(48) Baljon, A. R.; Robbins, M. O. A molecular view of bond rupture. *Comput. Theor. Polym. Sci.* **1999**, *9*, 35−40.
(49) Sides, S. W.; Grest, G. S.; Stevens, M. J. Large-Scale Simulation of Adhesion Dynamics for End-Grafted Polymers. *Macromolecules* **2002**, *35*, 566−573.
(50) Rottler, J. Fracture in glassy polymers: a molecular modeling perspective. *J. Phys.: Condens. Matter* **2009**, *21*, 463101.
(51) Everaers, R.; Karimi-Varzaneh, H. A.; Fleck, F.; Hojdis, N.; Svaneborg, C. Kremer-Grest Models for Commodity Polymer Melts: Linking Theory, Experiment, and Simulation at the Kuhn Scale. *Macromolecules* **2020**, *53*, 1901−1916.
(52) Senftle, T. P.; Hong, S.; Islam, M. M.; Kylasa, S. B.; Zheng, Y.; Shin, Y. K.; Junkermeier, C.; Engel-Herbert, R.; Janik, M. J.; Aktulga, H. M.; Verstraelen, T.; Grama, A.; van Duin, A. C. T. The ReaxFF reactive force-field: development, applications and future directions. *npj Computational Materials* **2016**, *2*, 15011.
(53) Stuart, S. J.; Tutein, A. B.; Harrison, J. A. A reactive potential for hydrocarbons with intermolecular interactions. *J. Chem. Phys.* **2000**, *112*, 6472−6486.
(54) Plimpton, S. J.; Thompson, A. P. Computational aspects of many-body potentials. *MRS Bull.* **2012**, *37*, 513−521.
(55) Plimpton, S. Fast Parallel Algorithms for Short-Range Molecular Dynamics. *J. Comput. Phys.* **1995**, *117*, 1−19.
(56) Humphrey, W.; Dalke, A.; Schulten, K. VMD: Visual molecular dynamics. *J. Mol. Graphics* **1996**, *14*, 33−38.
(57) Smith, G. D.; Paul, W. United Atom Force Field for Molecular Dynamics Simulations of 1,4-Polybutadiene Based on Quantum

https://doi.org/10.1021/acspolymersau.1c00023
ACS Polym. Au 2021, 1, 175−186

Chemistry Calculations on Model Molecules. *J. Phys. Chem. A* **1998**, *102*, 1200−1208.
(58) He, L.; Sewell, T. D.; Thompson, D. L. Molecular dynamics simulations of shock waves in cis −1,4-polybutadiene melts. *J. Appl. Phys.* **2013**, *114*, 163517.
(59) Jorgensen, W. L.; Madura, J. D.; Swenson, C. J. Optimized intermolecular potential functions for liquid hydrocarbons. *J. Am. Chem. Soc.* **1984**, *106*, 6638−6646.
(60) Belton, D. J.; Deschaume, O.; Perry, C. C. An overview of the fundamentals of the chemistry of silica with relevance to biosilicification and technological advances. *FEBS J.* **2012**, *279*, 1710−1720.
(61) There is an error in Table 1 of ref 45 in the part involving the Lennard−Jones parameters for CH_2 and CH. The σ_{ij} values in the published version of the table were copied from an analogous table in ref 58, where however they represented r_{ij}^0 values (distances of minimum potential energy). Thus, they should have been rescaled as follows: $\sigma_{ij} = 2^{-1/6} r_{ij}^0$. Despite of this error in the table, the simulations described in ref 45 are correct, as the σ_{ij} values in our LAMMPS input files had been rescaled correctly.
(62) Luo, Y.-R. *Handbook of Bond Dissociation Energies in Organic Compounds*; CRC Press: 2002; p 392. DOI: 10.1201/9781420039863.
(63) Neese, F. The ORCA program system. *Wiley Interdiscip. Rev.: Comput. Mol. Sci.* **2012**, *2*, 73−78.
(64) Emami, F. S.; Puddu, V.; Berry, R. J.; Varshney, V.; Patwardhan, S. V.; Perry, C. C.; Heinz, H. Force field and a surface model database for silica to simulate interfacial properties in atomic resolution. *Chem. Mater.* **2014**, *26*, 2647−2658.
(65) Fetters, L. J.; Lohse, D. J.; Richter, D.; Witten, T. A.; Zirkel, A. Connection between Polymer Molecular Weight, Density, Chain Dimensions, and Melt Viscoelastic Properties. *Macromolecules* **1994**, *27*, 4639−4647.
(66) Wolff, S. Chemical Aspects of Rubber Reinforcement by Fillers. *Rubber Chem. Technol.* **1996**, *69*, 325−346.
(67) Blume, A. Private communication after the seminar "A detailed view inside silica/silane coupling". Politecnico di Milano, June 2018.
(68) Greenwood, N. N.; Earnshaw, A. *Chemistry of the Elements*; Elsevier: 2012.
(69) Auhl, R.; Everaers, R.; Grest, G. S.; Kremer, K.; Plimpton, S. J. Equilibration of long chain polymer melts in computer simulations. *J. Chem. Phys.* **2003**, *119*, 12718−12728.
(70) Todd, B. D.; Daivis, P. J. *Nonequilibrium Molecular Dynamics: Theory, Algorithms and Applications*; Cambridge University Press: 2017.
(71) Raos, G. Application of the Christensen-Lo Model to the Reinforcement of Elastomers by Fractal Fillers. *Macromol. Theory Simul.* **2003**, *12*, 17−23.
(72) Clough, J. M.; Creton, C.; Craig, S. L.; Sijbesma, R. P. Covalent Bond Scission in the Mullins Effect of a Filled Elastomer: Real-Time Visualization with Mechanoluminescence. *Adv. Funct. Mater.* **2016**, *26*, 9063−9074.
(73) Diani, J.; Fayolle, B.; Gilormini, P. A review on the Mullins effect. *Eur. Polym. J.* **2009**, *45*, 601−612.
(74) Rycroft, C. H. VORO++: A three-dimensional Voronoi cell library in C++. *Chaos* **2009**, *19*, 041111.
(75) Caputo, S.; Hristov, V.; Nicola, A. D.; Herbst, H.; Pizzirusso, A.; Donati, G.; Munaò, G.; Albunia, A. R.; Milano, G. Efficient Hybrid Particle-Field Coarse-Grained Model of Polymer Filler Interactions: Multiscale Hierarchical Structure of Carbon Black Particles in Contact with Polyethylene. *J. Chem. Theory Comput.* **2021**, *17*, 1755−1770.
(76) Shen, J.; Liu, J.; Gao, Y.; Li, X.; Zhang, L. Elucidating and tuning the strain-induced non-linear behavior of polymer nanocomposites: a detailed molecular dynamics simulation study. *Soft Matter* **2014**, *10*, 5099−5113.
(77) Hattemer, G. D.; Arya, G. Viscoelastic Properties of Polymer-Grafted Nanoparticle Composites from Molecular Dynamics Simulations. *Macromolecules* **2015**, *48*, 1240−1255.
(78) Chao, H.; Riggleman, R. A. Effect of particle size and grafting density on the mechanical properties of polymer nanocomposites. *Polymer* **2013**, *54*, 5222−5229.
(79) Pfaller, S.; Possart, G.; Steinmann, P.; Rahimi, M.; Müller-Plathe, F.; Böhm, M. C. Investigation of interphase effects in silica-polystyrene nanocomposites based on a hybrid molecular-dynamics−finite-element simulation framework. *Phys. Rev. E: Stat. Phys., Plasmas, Fluids, Relat. Interdiscip. Top.* **2016**, *93*, 052505.

https://doi.org/10.1021/acspolymersau.1c00023
ACS Polym. Au 2021, 1, 175−186